Degradation analysis of dynamic properties for plain concrete structures under mixed-mode fracture conditions via an improved cohesive crack approach

Umberto De Maio, Daniele Gaetano, Fabrizio Greco
Department of Civil Engineering, University of Calabria, 87036 Rende (Italy)
umberto.demaio@unical.it, https://orcid.org/0000-0002-7363-0738
daniele.gaetano@unical.it, https://orcid.org/0000-0002-3857-8540
fabrizio.greco@unical.it, https://orcid.org/0000-0001-9423-4964

Raimondo Luciano
Department of Engineering, Parthenope University of Naples, 80133 Napoli (Italy)
raimondo.luciano@uniparthenope.it

Andrea Pranno
Department of Civil Engineering, University of Calabria, 87036 Rende (Italy)
andrea.pranno@unical.it, https://orcid.org/0000-0002-6925-2949

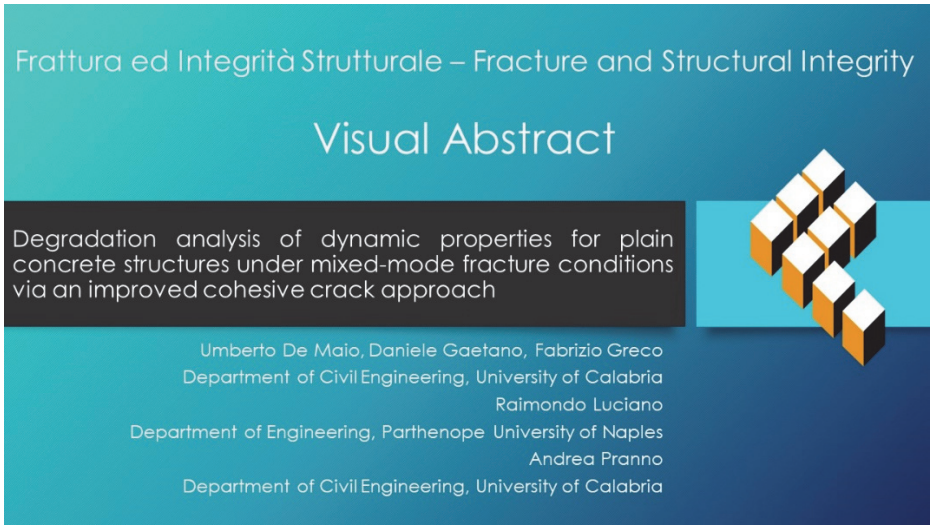

Citation: De Maio, U., Gaetano, D., Greco, F., Luciano, R., Pranno, A., Degradation analysis of dynamic properties for plain concrete structures under mixed-mode fracture conditions via an improved cohesive crack approach, Frattura ed Integrità Strutturale, 68 (2024) 422-439.

Received: 02.03.2024
Accepted: 21.03.2024
Published: 26.03.2024
Issue: 04.2024

KEYWORDS. Structural health monitoring, Concrete structures, Static and dynamic structural response, Cohesive zone model.

INTRODUCTION

Structural Health Monitoring (SHM) techniques have emerged as indispensable tools for ensuring the safety and longevity of civil infrastructure. These techniques involve the continuous or periodic monitoring of structural behavior to detect and diagnose damage thus mitigating the risk of structural failures and optimizing maintenance strategies. One of the key components of SHM is the utilization of numerical models to interpret monitoring data and assess structural health. These models, ranging from simple analytical formulations to complex finite element simulations, play a pivotal role in understanding the behavior of structures under various loading conditions and in predicting their response to damage. In the scientific literature, damage identification methodologies are typically categorized into data-based and model-based approaches [1–3]. Methods falling under the former category depend on static and dynamic data collected either on demand, periodically, or continuously over time during the inspection phase of monitored structures. These global parameters are subsequently contrasted with those recorded during the initial baseline phase, representing the undamaged structural state, to facilitate damage detection, localization, and magnitude estimation [4–6]. The reliability of data-based methods is also contingent upon the efficacy of software components employing signal-processing, pattern recognition algorithms, or statistical analyses to translate data acquired from sensors such as accelerometers, strain gauges, velocimeters, load cells, and fiber optic sensors into meaningful structural condition information [7–10]. Various techniques utilizing machine learning approaches [11–13], Support Vector Machines (SVM) [14,15], and data clustering methods [16,17] have been proposed for this purpose. On the other hand, model-based approaches involve the updating of finite element models (FEMs), according to which a set of parameters from an initial model representing the undamaged baseline condition of the monitored structure are adjusted to better match the actual structural state under damage [18,19]. This adjustment process entails the formulation of an optimization problem aimed at minimizing differences between the experimentally measured dynamic responses and those predicted by the numerical model. Upon achieving an optimal alignment, the location and extent of damage can be determined [20]. The effectiveness of model updating is strictly related to the chosen numerical model used to simulate the progressive development of damage. For instance, in [21], a simplified damage model which involves alteration of the elastic modulus within a narrow band surrounding existing cracks, is proposed to simulate stiffness degradation throughout the structure subjected to cracking processes. Similarly, elastic springs with equivalent stiffness are utilized along cracked sections to emulate the impact of damage on the structure, followed by modal analyses conducted with suitable adjustments to the spring conditions to align with experimentally obtained dynamic data [22]. More reliable numerical methods in terms of predicted structural nonlinear response rely on discrete and smeared fracture approaches. Discrete fracture methods, including cohesive models [23,24], have the main advantage of appropriately predicting the crack pattern induced by the applied loads, as well as the complex damage phenomena typical of plain and reinforced concrete (RC) structures. Moreover, they are versatile and applicable to different types of quasi-brittle materials, such as concrete elements [25] and fiber-reinforced composite materials [26–28], RC structures strengthened with FRP systems [29,30], and RC beams enhanced with nanomaterials embedded in the concrete matrix [31–33]. Additionally, they combine reliability, in terms of expected results, and lower computational costs. On the other hand, smeared damage approaches benefit from appropriate constitutive laws and bond-slip relations to accurately simulate the softening behavior resulting from crack evolution and the bond behavior between concrete/steel and concrete/FRP [34–36]. Nevertheless, while these models excel in predicting load-carrying capacity, they are less adept at accurately reproducing realistic crack patterns due to the inherent loss of features during the smoothing process. However, a damage identification method for analyzing concrete structures, regardless of whether it adopts a smeared or discrete fracture approach, necessitates an accurate numerical strategy. For instance, employing multiscale approaches or advanced finite element methods [37] in tandem with a well-designed monitoring campaign is imperative to comprehensively analyze the behavior of existing structures and understand the complexities of potential failure mechanisms. Numerous experimental and numerical works available in the scientific literature are mainly focused on RC structural elements. In particular, an experimental method based on the static moment–rotation relationship evaluation over a beam short subsection, is proposed to better understand the non-linear behaviour of damaged concrete beams during low-amplitude vibration [38,39].

In the work [40], a reinforced concrete (RC) slab underwent short-duration concentrated impact loads, and its dynamic characteristics in both virgin and damaged conditions were investigated using two signal processing techniques: Fast Fourier Transform (FFT) and Hilbert Huang Transform (HHT). The analyses revealed percentage reductions in modal frequency corresponding to varying degrees of damage, and the frequency–damage relationship was estimated based on a 3-element partitioned beam model, demonstrating close agreement between semi-empirical and experimental results, with a 30% frequency reduction observed from the virgin state to yield. A novel damage assessment procedure, proposed in [41], utilizes changes in non-linear vibration characteristics obtained from computational models, employing a constitutive model derived from laboratory compressive strength tests and implemented in finite element modeling. Incremental static damage is

simulated and harmonic excitation detects non-linear behavior, enabling the proposal of a damage detection method independent of baseline data. Experimental validation demonstrates the method's simplicity, computational efficiency, agreement with cracked vibration behavior studies, and potential for addressing inverse engineering problems in structural health monitoring of RC structures. Interesting results are obtained in [42], where linear and nonlinear acoustical experiments were conducted on a reinforced concrete (RC) beam subjected to gradually induced damage through static loading tests. Specifically, experimental modal analysis (EMA) at varying damage levels revealed a progressive reduction in bending stiffness along the beam, with increasing damage showing strong amplitude dependence in linear dynamic behavior. Resonant frequencies and damping ratios were measured after each loading step, using both frequency and time domain techniques, to quantify nonlinearity as a function of damage.

In the context of the structural health monitoring procedures based on the coupling between numerical models and experimental data, in this work, a numerical model has been developed to investigate the crack-induced degradation of vibration characteristics in plain concrete structures under mode I and mode II fracture conditions. In order to take into account all complex nonlinear phenomena, such as concrete crushing, concrete plasticity, and the friction effect during the unloading phase, an extension of the cohesive model proposed by some of the authors in [25] has been implemented in a 2D finite element framework. In particular, a cohesive zone model, used to predict the crack onset and propagation in the concrete phase has been successfully applied to analyze the structural behavior of concrete elements subjected to cycling loading conditions, taking into account both concrete plasticity and contact/friction effects between the crack faces during the unloading stage. The static and dynamic behaviors of concrete beams under general loading conditions have been studied evaluating mode shapes by solving small amplitude-free oscillations problems at the final point of each unloading path. Finally, the variation of the natural vibration frequencies as the damage level increases has been investigated, and the most common dynamic damage indicators have been calculated to assess the location and magnitude of the damage within the analyzed elements.

STATIC AND DYNAMIC ANALYSIS OF PLAIN CONCRETE STRUCTURES UNDER LOADING/UNLOADING PROCESSES

In this section, the numerical strategy proposed to analyze the degradation of the dynamic properties of plain concrete specimens, has been briefly introduced. Specifically, the nonlinear process induced by the crack propagation is simulated by a diffuse cohesive approach, proposed by some of the authors in [31], which has been here enhanced to suitably predict the frictional effects arising during the closure phenomenon of the crack faces in a compression loading state. Moreover, the dynamic properties of the damaged concrete specimens are detected by solving the modal model of the structural system thus obtaining natural vibration frequencies and mode shapes of the concrete specimens [25]. The proposed strategy is implemented in a 2D finite element framework by using the commercial software COMSOL Multiphysics.

Nonlinear fracture simulation of plain concrete specimens

The nonlinear behavior of plain concrete specimens has been analyzed by using an inter-element fracture model, according to which cohesive interfaces are inserted between the bulk elements of a standard FE mesh within the critical zone subjected to damage. The mechanical behavior of the cohesive tractions, for monotonic and cyclic tensile loads, is described by a traction-separation law of the kind $\boldsymbol{t}_{coh} = (1-D)\boldsymbol{K}^0[\![\boldsymbol{u}]\!]$, depending on an isotropic damage variable D. In order to analyze the cracking processes in concrete structures subjected to loading/unloading conditions, the numerical formulation should incorporate concrete plasticity. As introduced by some of the authors in [25], such effect is considered by adopting the plastic contribution δ_n^p and δ_s^p for the normal and the tangential components of the displacement jump $[\![\boldsymbol{u}]\!]$. Therefore, the components of the cohesive traction vector can be expressed as follows:

$$\begin{Bmatrix} t_n \\ t_s \end{Bmatrix} = (1-D)\begin{bmatrix} K_n^0 & 0 \\ 0 & K_s^0 \end{bmatrix}\begin{Bmatrix} (\delta_n - \delta_n^p)\dfrac{\delta_n^{\max}}{\delta_n^{\max} - \delta_n^p} \\ (\delta_s - \delta_s^p)\dfrac{\delta_s^{\max}}{\delta_s^{\max} - \delta_s^p} \end{Bmatrix} \tag{1}$$

Such plastic contribution have been set as a fraction of the maximum values of the normal displacement jump, i.e. $\delta_n^p = \gamma \delta_n^{\max}$. The parameter γ is a linear function rely upon the ratio between the actual tensile stress and the critical tensile strength of the material (f_t / f_{tc}) and it has been defined by a calibration procedure to match the experimental results given in [43]. In Eqn. (1), the scalar damage variable follows an exponential function, governed by the parameters α as follows:

$$D = \begin{cases} 0 & \delta_m^{\max} \le \delta_m^0 \\ 1 - \dfrac{\delta_m^0}{\delta_m^{\max}} \left\{ 1 - \dfrac{1 - \exp\left[-\alpha \left(\dfrac{\delta_m^{\max} - \delta_m^0}{\delta_m^f - \delta_m^0} \right) \right]}{1 - \exp(-\alpha)} \right\} & \delta_m^0 \le \delta_m^{\max} \le \delta_m^f \\ 1 & \delta_m^{\max} > \delta_m^f \end{cases} \tag{2}$$

in which the parameters δ_m^f and δ_m^0 represent the limit values that the equivalent displacement jumps reach at the complete decohesion and at the onset of the cracks, respectively. The maximum value of such equivalent displacement jump, throughout the load history, is indicated by $\delta_m^{\max}$ in Eqn. (2).

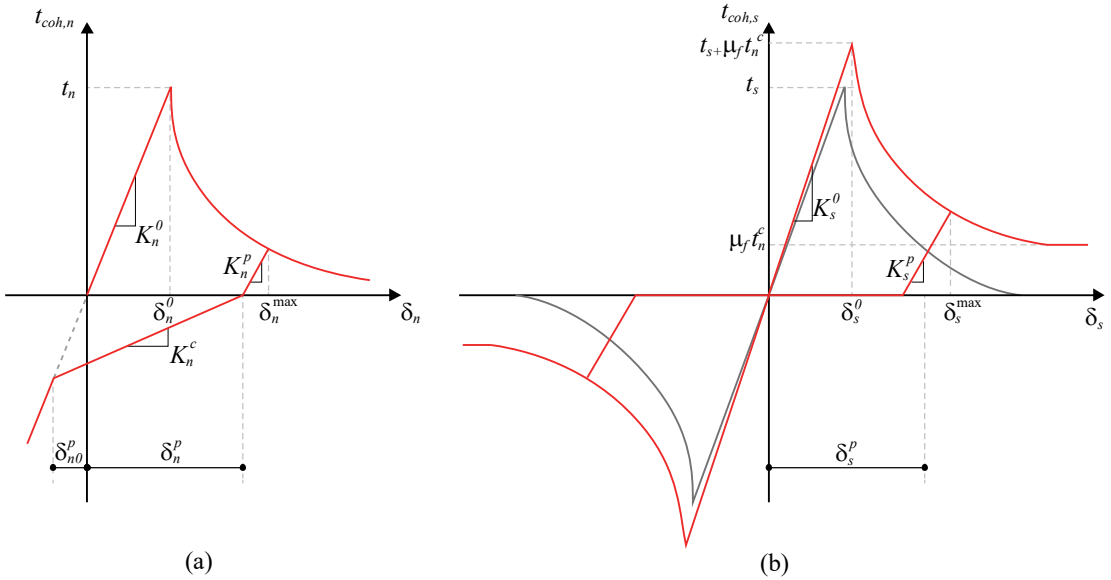

Figure 1: Traction-separation laws for Mode I (a) and Mode II (b) fracture conditions.

Fig. 1a and Fig. 1b illustrate the complete traction-separation laws for Mode I and Mode II fracture processes both characterized by a plastic stiffness in the unloading stage, thus defined:

$$K_i^p = \frac{(1-D) K_i^0 \delta_i^{\max}}{\delta_i^{\max} - \delta_i^p} \quad i = n, s \tag{3}$$

where K_i^0 denoting the initial elastic stiffness, in its normal $(i = n)$ and tangential $(i = s)$ components.
During the unloading stage, in order to simulate the effect of the partial contact between crack faces, induced by the presence of aggregates in the concrete phase, the following expression of the cohesive normal stress has been introduced:

$$t_n^c = \begin{cases} K_n^c\left(\delta - \delta_n^p\right) & \delta_{n0}^p \le \delta_n \le \delta_n^p \\ K_n^0 \delta_n & \delta_n < \delta_{n0}^p \end{cases} \tag{4}$$

where K_n^c is the normal tangent stiffness computed by an adaptive formulation when an inversion in the sign of the cohesive stresses, from tensile to compressive during the unloading phase, is registered:

$$K_n^c = \frac{K_n^0 + \left(1-\gamma_n\right)\beta K_n^p}{1+\beta} \tag{5}$$

where the scalar parameter β, set as 225 after the calibration procedures performed on experimental works [43,44], reduces the initial normal stiffness K_n^0 as the damage increases. The interpenetration phenomenon between cohesive elements is prevented through a contact constraint that is active when the displacement reaches the limit values of:

$$\delta_{n0}^p = -\frac{\delta_n^p K_n^c}{K_n^c + K_n^0} \tag{6}$$

The numerical formulation is further improved by incorporating the friction effects in the mode II traction-separation law, in order to adequately model the constitutive behavior of the cohesive elements during the unloading phase characterized by compression states, especially when a mixed-mode fracture condition is analyzed. In detail, according to the Coulomb-type frictional model, the total cohesive tangential stress t_s^{tot} is defined as a summation of the cohesive contributions t_s, expressed by Eqn. (1) and the friction contribution t_s^{fric}, when a compression state is reached, as follows:

$$t_s^{tot} = \begin{cases} t_s^c - sgn\left(\delta_s\right)\mu_f t_n^c & \delta_n \le \delta_n^p \\ t_s & \delta_n > \delta_n^p \end{cases} \tag{7}$$

where μ_f is the friction parameter that assumes, according to [45], two different values:

$$\mu_f = \begin{cases} \mu_0\left(\left|\delta_s\right| / \delta_s^0\right) & \delta_m^{\max} \le \delta_m^f \\ \mu_0 & \delta_m^{\max} > \delta_m^f \end{cases} \tag{8}$$

in which μ_0 is the friction coefficient, set equal to 0.3.

Dynamic property evaluation of plain concrete structures

The dynamic response of reinforced concrete structures under defined damage states is determined by solving the small amplitude free oscillation problem of the discretized structural model using a displacement-based finite element approach, similar to that employed in [25]. Linearized equations of motion are derived for undamped dynamic systems, with the stiffness matrix considering nonlinearities from cohesive constitutive laws due to damage, plasticity, and partial contact phenomena. The solution yields natural vibration frequencies and mode shapes, represented by the spectral and modal matrices, respectively, forming the "Modal Model" of the structural system, which must be updated for each damage level associated with varying loading and unloading states.

In particular, the well-known second-order differential equation for the motion is expressed as follows:

$$\mathbf{M}\mathbf{q}(t) + \mathbf{K}\left(\mathbf{q}^{st}\left(\tau, \tau \le t\right)\right)\mathbf{q}(t) = \mathbf{0} \tag{9}$$

being $\mathbf{M}$ and $\mathbf{K}$ are the symmetric and positive defined mass and tangent stiffness matrix, respectively. $\mathbf{q}(t)$ is a vector of order equal to the number of degrees of freedom of the considered system where the generalized nodal displacements are listed. The stiffness matrix $\mathbf{K}$ is expressed as a function of the damage $\mathbf{q}^{sf}(\tau, \tau \le t)$ detected by the previously performed quasi-static analysis. The symmetric eigenvalue problem in free oscillations can be simplified into the following canonical form for the i-th mode:

$$\left[\mathbf{K} - \omega_i^2 \mathbf{M}\right]\mathbf{u}_i = \mathbf{0} \tag{10}$$

which provides N positive real solutions ($\omega_1^2, \omega_2^2 ... \omega_N^2$), with N representing the dimension of the vector $\mathbf{u}_i$, denoting the natural vibration frequencies of the undamped system corresponding to the N real mode shapes. The solution of the free oscillation problem can be expressed in terms of spectral matrix $\mathbf{\Lambda}$ and modal shape matrix, $\mathbf{\Psi}$ as follows:

$$\begin{aligned} \mathbf{\Lambda} &= diag\left(\omega_1^2 \quad \omega_2^2 \quad ... \quad \omega_N^2\right), \\ \mathbf{\Psi} &= \left(\mathbf{\Psi}_1 \quad \mathbf{\Psi}_2 \quad ... \quad \mathbf{\Psi}_N\right). \end{aligned} \tag{11}$$

The natural vibration frequencies are obtained through the following expression: $f_i = \omega_i / 2\pi$, thus defining the so-called "Modal Model" which describes the structural system using its modal properties.

NUMERICAL RESULTS

In this section, the proposed numerical strategy has been employed to analyze the dynamic properties degradation of plain concrete specimens subjected to mixed-mode fracture conditions. In particular, two different tests are simulated. The former is a plain concrete specimen subjected to a pure Mode-I fracture condition, whereas the latter involves the general mixed-mode fracture condition. The main goal of the analyses is to study the damage effects on both load-carrying capacity and modal characteristics of the simulated concrete elements.

Static and dynamic response of a concrete specimen under mode-I fracture conditions

A three-point bending numerical test is performed involving a plain concrete beam whose geometry and boundary conditions, expressed as a function of height $H = 0.2\,\text{m}$, are shown in Fig. 2(a). The elastic and strength properties of the beam were taken equal to those used in [46]. In particular, Young's modulus and Poisson's ratio of concrete are equal to $E = 30\,\text{GPa}$ and $\nu = 0.18$ respectively, while the cohesive parameters required by the interface law to simulate crack initiation and propagation are shown in Tab. 1.

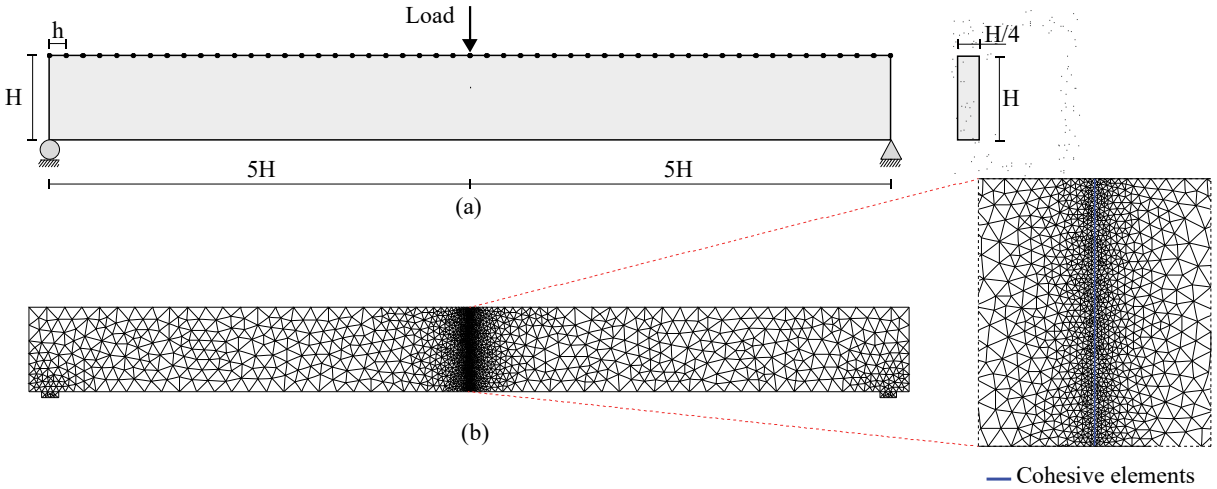

Figure 2: Geometry and boundary conditions (a); adopted finite element mesh (b) for the three-point bending test.

K_n^0 [N/mm³]	K_s^0 [N/mm³]	σ_{max} [MPa]	τ_{max} [Mpa]	G_{Ic} [N/m]	G_{IIc} [N/m]	α	β
1.061e6	8.821e5	3.33	3.33	124	124	5	225

Table 1: Cohesive parameters required by the cohesive traction-separation law.

The values of the initial stiffnesses for the interface law have been calculated by means of the micromechanical calibration methodology proposed in [25] admitting an apparent reduction of the Young's modulus of 2% for the adopted topology and size of the mesh. The mode II parameters, i.e. strength and fracture energy, have been chosen equal to mode I parameters in order to avoid over-resistance effects associated with artificial mesh-induced local mixed-mode state activation. It is important to note that, in order to reduce the computational effort, in the numerical simulations the cohesive elements are inserted only along the vertical line coinciding with the expected path of the main crack (Fig. 2(b)) due to the symmetry for both geometry and boundary conditions. An unstructured mesh (i.e. Delaunay), consisting of three-node planar elements for the solid phase, with a maximum elements size of 42 mm, and zero-thickness four-node elements, arranged along the vertical direction in a number of 30, for the cohesive interfaces, have been used for all simulations.
Quasi-static loading/unloading analyses are performed under plane stress assumption using a displacement-based control algorithm with a displacement increment of 5e-3 mm. The obtained results, in terms of load-deflection curve, are reported in Fig. 3. In particular, at 6 load levels, evaluated as a fraction of the failure load, the tested specimen has been subjected to an unloading stage. They are denoted as: L1, L2, L3, L4, L5, and L6, corresponding to a deflection value of 0.3, 0.515 (deflection at peak load), 0.55, 0.6, 0.8, and 1 mm respectively. The unloading paths have been stopped once a zero value of the load acting on the beam has been reached (points L1', L2', L3', L4', L5', L6' of Fig. 3).

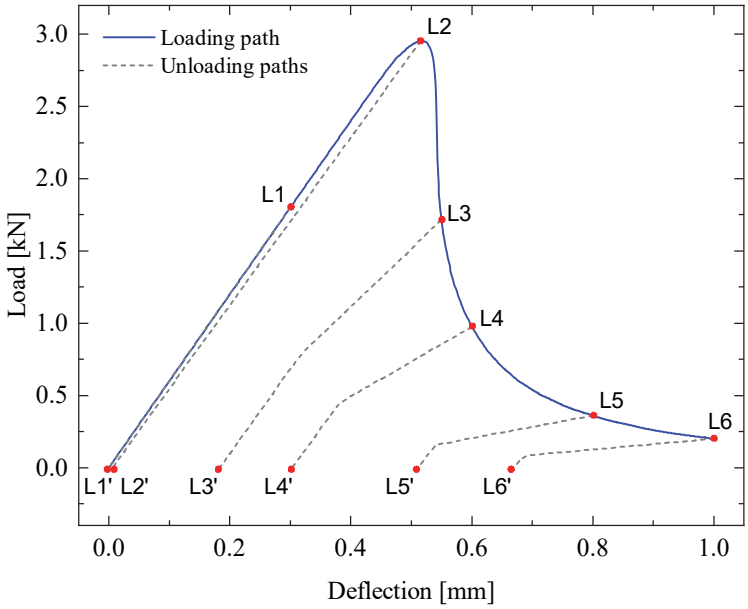

Figure 3: Load-deflection curve with the performed unloading paths.

The obtained loading curve reflects the typical behavior of quasi-brittle materials with a linearly elastic branch until the peak load, followed by the softening behavior characterized by a fast reduction of the load level. We can note that, along the unloading paths corresponding to different damage levels in the softening branch, where the main crack is almost fully developed, distinct tangent stiffnesses can be observed. This reflects the model's capabilities to predict the intermediate contact state between open and closed cracks, as well as frictional effects resulting from the presence of aggregates that prevent complete crack closure.
Subsequently, the dynamic response of the plain concrete specimen in the presence of damage, previously detected by the quasi-static analysis, is determined by solving the problem of free oscillations of small amplitude, superimposed on the fixed damage configurations. The damage scenarios are associated with the final point of the unloading stages highlighted with red point in Fig. 3. The dynamic behavior in the regime of free oscillations is studied with reference to the damaged

framework reached during the unloading stage (points L1'-L6' in Fig. 3). This configuration takes into account the contact phenomena, as well as the friction effects, due to the partial closure of cracks that occur during the unloading phase.
Tab. 2 shows the variation of the natural vibration frequencies, obtained by the linearized modal analysis at the final point of the unloading branches, as a function of the damage, together with the relative percentage changes with respect to the undamaged configuration for each natural vibration mode. Since at the unloading phase, as previously explained, the stiffening effect of the partial crack closure is taken into account, the reduction of the natural frequencies is quite small. The maximum reduction value of 7.40% comes up at the last unloading stage for the 5th natural vibration mode. However, it should be noted that the damage configurations obtained once the peak load of the system has been exceeded, are difficult to achieve due to the unstable fracture process behavior of the specimen, which is typical in quasi-brittle materials like plain concrete beams (i.e. without any steel reinforcements).

Damage Levels	f_1 [Hz]	$\Delta f_1/f^0_1$ [%]	f_2 [Hz]	$\Delta f_2/f^0_2$ [%]	f_3 [Hz]	$\Delta f_3/f^0_3$ [%]	f_4 [Hz]	$\Delta f_4/f^0_4$ [%]	f_5 [Hz]	$\Delta f_5/f^0_5$ [%]
Undamaged	77.23	0.00	245.19	0.00	379.94	0.00	671.05	0.00	974.13	0.00
L1'	77.23	0.00	245.19	0.00	379.94	0.00	671.05	0.00	974.13	0.00
L2'	77.01	0.28	245.19	0.00	379.93	0.00	668.77	0.34	973.76	0.04
L3'	76.82	0.53	244.71	0.20	378.87	0.28	665.71	0.80	962.87	1.16
L4'	76.62	0.79	243.76	0.58	376.82	0.82	663.63	1.11	945.34	2.96
L5'	75.86	1.78	241.97	1.31	369.54	2.74	656.05	2.24	922.70	5.28
L6'	75.15	2.69	240.48	1.92	364.76	4.00	653.08	2.68	902.04	7.40

Table 2: Percentage variation of the natural vibration frequencies, as the damage level increases, in the unloading phase.

The results in terms of degradation of natural vibration frequencies, normalized with respect to the value obtained for the undamaged configuration, are also reported in Fig. 4.

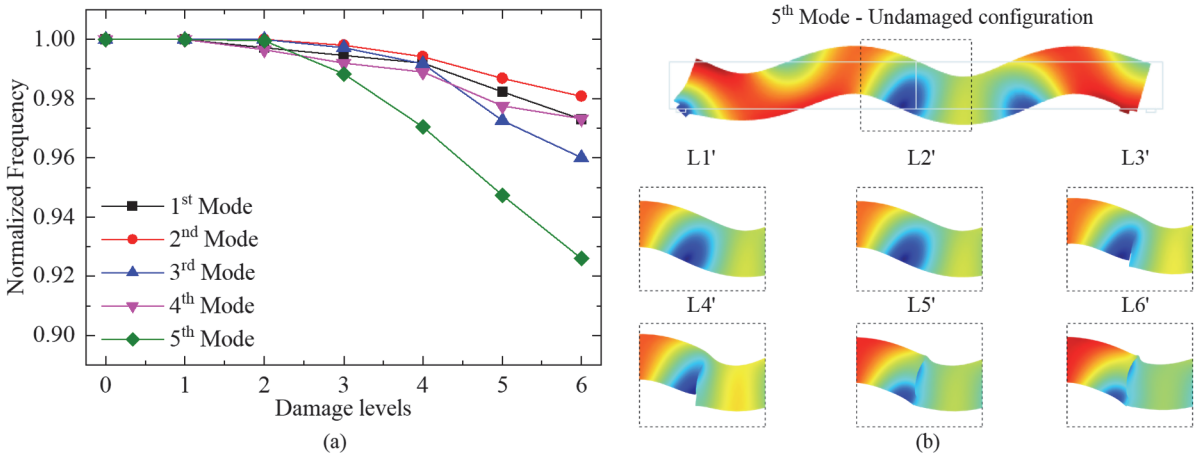

Figure 4: Variation of the normalized natural vibration frequencies for the first five mode shapes as the damage level increases.

In order to evaluate the effects of the progressive damage on the dynamic characteristic of plain concrete structures, the "Modal Assurance Criterion" (MAC) [47], has been used. Since the damage in structural elements induces a variation in the natural vibration modes, through the MAC values it is possible to obtain a scalar measure of the damage as a function of the correlation between the natural vibration modes before and after the damage occurrence. Such an indicator is expressed as follows:

$$MAC_{ij} = \frac{\left(\boldsymbol{\varphi}_{i,0}^{T}\boldsymbol{\varphi}_{j,d}\right)^{2}}{\left(\boldsymbol{\varphi}_{i,0}^{T}\boldsymbol{\varphi}_{,0}\right)\left(\boldsymbol{\varphi}_{j,d}^{T}\boldsymbol{\varphi}_{j,d}\right)} \tag{12}$$

where $\boldsymbol{\varphi}_{i,0}$ is the component vector in the undamaged configuration of the i-th vibration mode, while $\boldsymbol{\varphi}_{j,d}$ is the component vector in the damaged configuration of the j-th mode. Tab. 3 reports the MAC coefficients evaluated for the different damage levels. Such coefficients correlate the undamaged beam's natural modal shapes for the first five modes with the corresponding damaged ones (L1'-L6'). These values provide a measure of consistency between the two sets of modal vectors, undamaged and damaged. A unit value of the MAC coefficient corresponds to a perfect correlation between the considered two modes, while a value approaching zero indicates a complete inconsistency between the analyzed modal shapes, thus highlighting damage in the considered configuration. The obtained MAC coefficients have been determined with a normalization of the vibration modes through the mass matrix.

It is important to remind that all the modes are related to the unloaded condition. According to the results reported in Tab. 3, we may note that as the level of damage increases, the correlation between the mode in the damaged configuration and the relatively undamaged one, decreases. This is evidenced by the diagonal coefficients of the MAC matrix (MAC_{ii}), which increasingly diverge from unity as damage levels increase.

Undamaged – L1'				
1.0000	0.0944	0.0359	0.0008	0.0102
0.0944	1.0000	0.6439	0.0315	0.0048
0.0359	0.6439	1.0000	0.0240	0.0216
0.0008	0.0315	0.0240	1.0000	0.1170
0.0102	0.0048	0.0216	0.1170	1.0000

Undamaged – L2'				
1.0000	0.0944	0.0359	0.0008	0.0102
0.0946	1.0000	0.6438	0.0313	0.0049
0.0359	0.6439	1.0000	0.0241	0.0213
0.0008	0.0315	0.0240	1.0000	0.1201
0.0102	0.0048	0.0216	0.1167	1.0000

Undamaged – L3'				
1.0000	0.0944	0.0361	0.0008	0.0094
0.0933	1.0000	0.6448	0.0324	0.0046
0.0368	0.6452	1.0000	0.0239	0.0189
0.0007	0.0311	0.0229	1.0000	0.1248
0.0104	0.0051	0.0227	0.1053	0.9987

Undamaged – L4'				
0.9999	0.0938	0.0357	0.0008	0.0089
0.0922	0.9999	0.6469	0.0338	0.0041
0.0376	0.6469	0.9999	0.0236	0.0170
0.0007	0.0311	0.0220	0.9980	0.1255
0.0106	0.0057	0.0237	0.0945	0.9939

Undamaged – L5'				
0.9999	0.0944	0.0341	0.0006	0.0173
0.0991	0.9998	0.6479	0.0199	0.0164
0.0335	0.6431	0.9986	0.0345	0.0297
0.0005	0.0333	0.0214	0.9928	0.2167
0.0092	0.0065	0.0284	0.1502	0.9736

Undamaged – L6'				
0.9998	0.0938	0.0319	0.0007	0.0228
0.1003	0.9995	0.6498	0.0176	0.0236
0.0330	0.6406	0.9974	0.0361	0.0388
0.0004	0.0359	0.0219	0.9877	0.2438
0.0089	0.0073	0.0302	0.1635	0.9495

Table 3: Modal Assurance Criterion (MAC) for the investigated damage levels with reference to the undamaged configuration.

However, these deviations are not particularly significant; in fact, the maximum relative percentage deviation is 5 % and is found at the last damage level L6' for mode number 5. Moreover, at the same damage level, the higher modes generally show less correlation than the others. On the other hand, as the level of damage increases, the correlation between different

modes increases, i.e. the off-diagonal MACij coefficients take on values gradually greater than the initial one due to the approximate orthogonality between modes. This behavior is related to the expression used for the evaluation of MACs coefficients (Eqn. (9)) that is evaluated with reference to a reduced number of degrees of freedom and displacement directions concerning those for which the orthogonality condition is imposed.

Subsequently, to detect the damage position in the tested specimen, the modal curvature (MC) criterion [48] has been employed. In particular, the curvature φ''_{ij} of the modal shape at the generic *i*-th coordinate, has been evaluated for each considered damage level, by using the following expression:

$$MC = \varphi''_{ij} = \frac{\varphi_{(i-1)j} - 2\varphi_{(ij)} + \varphi_{(i+1)j}}{h^2} \tag{13}$$

where φ_{ij} is the displacement at the *i*-th coordinate of the *j*-th modal shape while *h* denotes the distance between two consecutive coordinates and set equal to 42 mm.

Fig. 5 shows the MCs at the different damage levels in the unloading phase (L1'-L6') for the investigated mode shapes considering 51 equidistant points located along the upper edge of the specimen, starting from the left-hand support. The values have been normalized with respect to the value of the maximum curvature obtained by the individual modes in the undamaged configuration. For each mode, as the damage level increases, the curvature shows an increasing peak in proximity to the crack. In particular, the curvature values deviate significantly from those obtained from the undamaged modal shape at points very close to the crack, resulting in noticeable changes in slope. This behavior becomes more pronounced as the level of damage increases, particularly when the crack is nearly fully developed, thus demonstrating the effectiveness of the proposed numerical strategy also in the detection of damage in plain concrete structures.

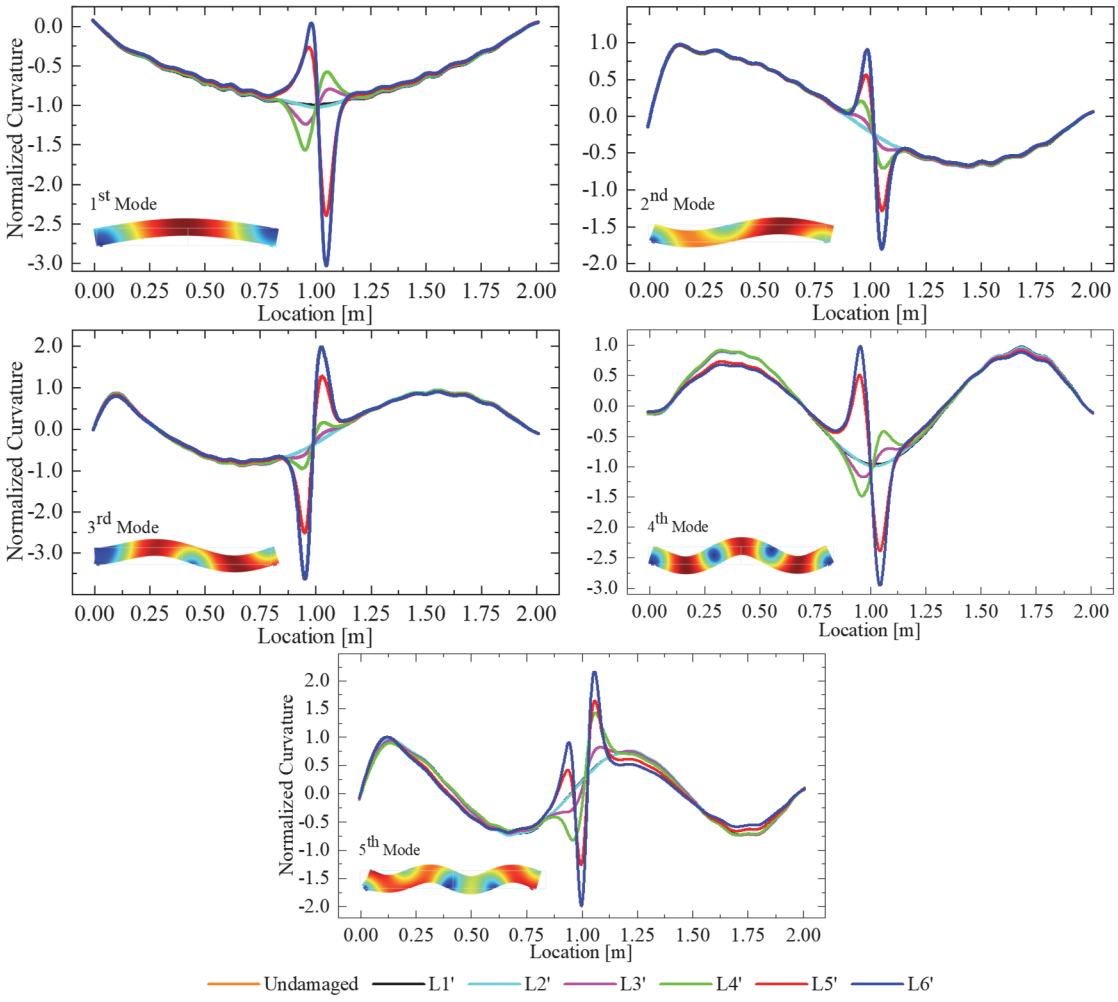

Figure 5: Modal Curvature (MC) damage factor of the first five mode shapes for all investigated damage levels at the unloading phase.

Static and dynamic response of a concrete specimen under mixed-mode fracture conditions

The proposed model is here employed to predict the degradation of modal properties of a concrete specimen subjected to general mixed-mode fracture conditions. The analyses refer to a non-symmetric three-point bending test involving a plain concrete notched beam experimentally analyzed by [49]. The geometry of the beam, expressed as a function of the beam height D equal to 75 mm, as well as the unstructured mesh used for the numerical simulations, are reported in Fig. 6. Assuming a linear elastic behavior for the bulk elements, a Young's Modulus of $E = 38$ GPa and a Poisson's ratio of $\nu = 0.20$ have been set, according to the parameters reported in [49]. Tab. 4, instead, reports the inelastic parameters chosen for the cohesive interfaces. As shown in Fig. 6, in order to reduce the degrees of freedom of numerical simulations, the cohesive elements, highlighted in blue in Fig. 6(b), have been included only in the area where damage could potentially evolve. As performed for the mode I loading conditions test, a Delaunay tessellation, with a maximum size of 18 mm and 2 mm for the bulk and cohesive elements respectively, has been used for the finite element mesh.

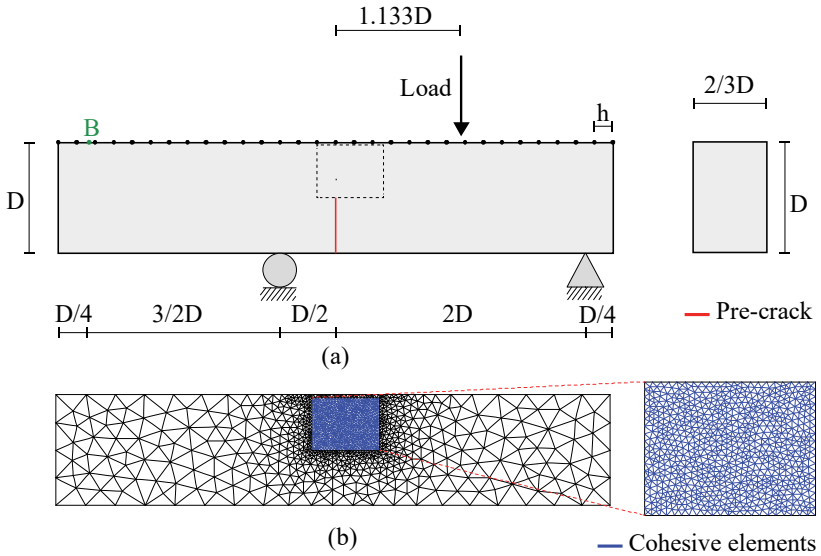

Figure 6: Geometry and boundary conditions (a) and finite element mesh (b) used for the non-symmetric three-point bending test.

K_n^0 [N/mm³]	K_s^0 [N/mm³]	σ_{max} [MPa]	τ_{max} [MPa]	G_{Ic} [N/m]	G_{IIc} [N/m]	α	β
5.492e6	2.746e6	3.00	3.00	69	69	5	225

Table 4: Cohesive parameters required by the adopted traction-separation law.

A quasi-static numerical simulation to predict the static response in terms of load-carrying capacity, has been performed assuming a plane stress condition and a displacement-based control algorithm with an increment of 5e-4 mm. Similarly to that carried out in the mode-I fracture test, a loading/unloading process has been imposed on the concrete specimen. In particular, at 6 values of displacement of point B reported in (Fig. 6(a)), i.e., 0.01, 0.0575 (corresponding to the peak load), 0.08, 0.12, 0.16 and 0.2 mm, 6 unloading stages, denoted as L1, L2, …, L6, are performed. It is worth noting that, such unloading processes are performed by decreasing the load level down to 0 kN (reaching points L1', … L6') starting from the load levels corresponding to the previously-mentioned displacements of Point B.

The obtained load versus displacement of the point B curve- is reported in Fig. 7. It can be seen that, at the final step of the first two unloading paths (L1 and L2), very small residual plastic deformations are predicted. On the other hand, considering the unloading paths starting from the load levels in the softening branch, the permanent residual deformations increase since the predicted crack is almost fully developed. Moreover, after a certain load level in the unloading path, we can note a stiffer structural behavior induced by the contact effects of the partially closed crack faces occurring in the cracked specimen. Such a static analysis has provided the damaged structural configurations (one for each considered damage level L1', … L6') on which the dynamic analyses were performed in order to assess the corresponding modal properties.

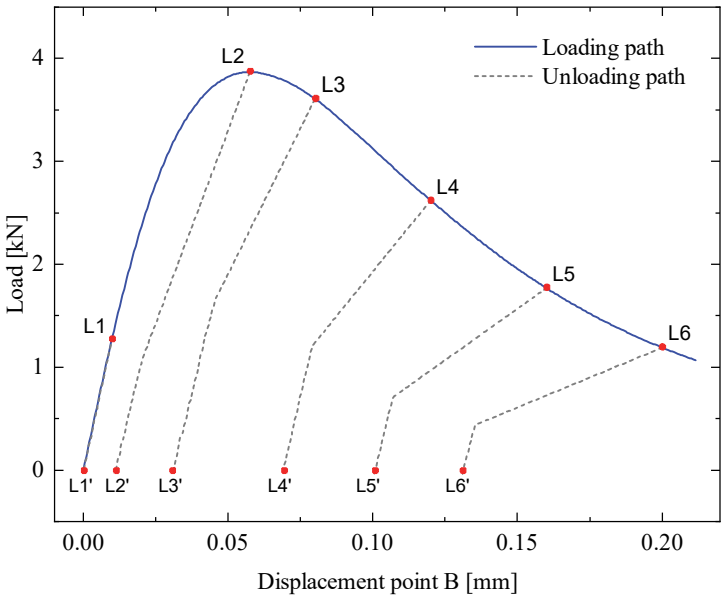

Figure 7: Load-displacement curve for the non-symmetric three-point bending test with the performed unloading paths.

Now, a linearized eigenvalue problem has been solved at the endpoint of each unloading path in order to take into account the effects of the complex nonlinear phenomena, such as concrete plasticity and partial crack closure behavior, on the natural vibration frequencies. The obtained results in terms of frequencies and their variations with respect to the undamaged configuration are reported in Tab. 5.

Damage Levels	f_1 [Hz]	$\Delta f_1/f^0_1$ [%]	f_2 [Hz]	$\Delta f_2/f^0_2$ [%]	f_3 [Hz]	$\Delta f_3/f^0_3$ [%]	f_4 [Hz]	$\Delta f_4/f^0_4$ [%]	f_5 [Hz]	$\Delta f_5/f^0_5$ [%]
Undamaged	632.86	0.00	2448.2	0.00	3423.5	0.00	5252.3	0.00	6696.2	0.00
L1’	632.86	0.00	2448.2	0.00	3423.5	0.00	5252.3	0.00	6696.2	0.00
L2’	601.79	4.91	2422.6	1.05	3230.3	5.64	5114.5	2.62	6674.7	0.32
L3’	581.09	8.18	2406.0	1.72	3191.7	6.77	5039.9	4.04	6653.1	0.64
L4’	588.6	6.99	2399.1	2.01	3190.3	6.81	5012.5	4.57	6623.5	1.09
L5’	567.27	10.36	2368.6	3.25	3071.9	10.27	4896.7	6.77	6582.6	1.70
L6’	546.21	13.69	2329.3	4.86	2988.7	12.70	4767.2	9.24	6545.2	2.26

Table 5: Percentage variation of the natural vibration frequencies, as the damage level increases, in the unloading phase for the non-symmetric three-point bending test.

The reduction of the natural vibration frequencies is not monotonically increasing for higher vibration modes. In fact, as reported in Tab. 5, the greatest reduction occurs for modes 1 and 3, which have frequency variation values of 13.69% and 12.70%, respectively. Such behavior is related to the peculiarity of the mixed-mode test of non-symmetric boundary conditions imposed on the analyzed concrete beam.

As is well known, the frictional effects become more prominent in all those cases where mixed-mode loading conditions are employed. To this end, in addition to the analysis of the frequency degradation, an interesting comparison in terms of variation of natural vibration frequencies predicted by the proposed model and by the same model without taking into account frictional effects, is reported in Fig. 8.

We can see that, the general trend is such that the contribution of the friction tends to increase the natural vibration frequencies and therefore to attenuate their degradation as the damage level increases, thus suitably simulating the real behavior of concrete structures. Such a behavior, is further pronounced by the contact between the crack faces characterized by a partial closure due to the presence of the aggregates. Small exceptions occur only for a few damage levels in some

vibration modes (see mode shapes number 1 and 4 of Fig. 9), characterized mainly by mode shapes that involve the free portion of the beam, beyond the left-hand support, and therefore do not involve the area affected by the growth of the damage. As a result, since the portion of the beam outside the cohesive zone is characterized by a linear elastic behavior, the friction effects are partially activated and are not high enough to generate a relatively large increase in the vibration frequencies. In fact, for the fourth mode, the frequency values associated with the cohesive model including the effects of friction are almost equal to those without ones.

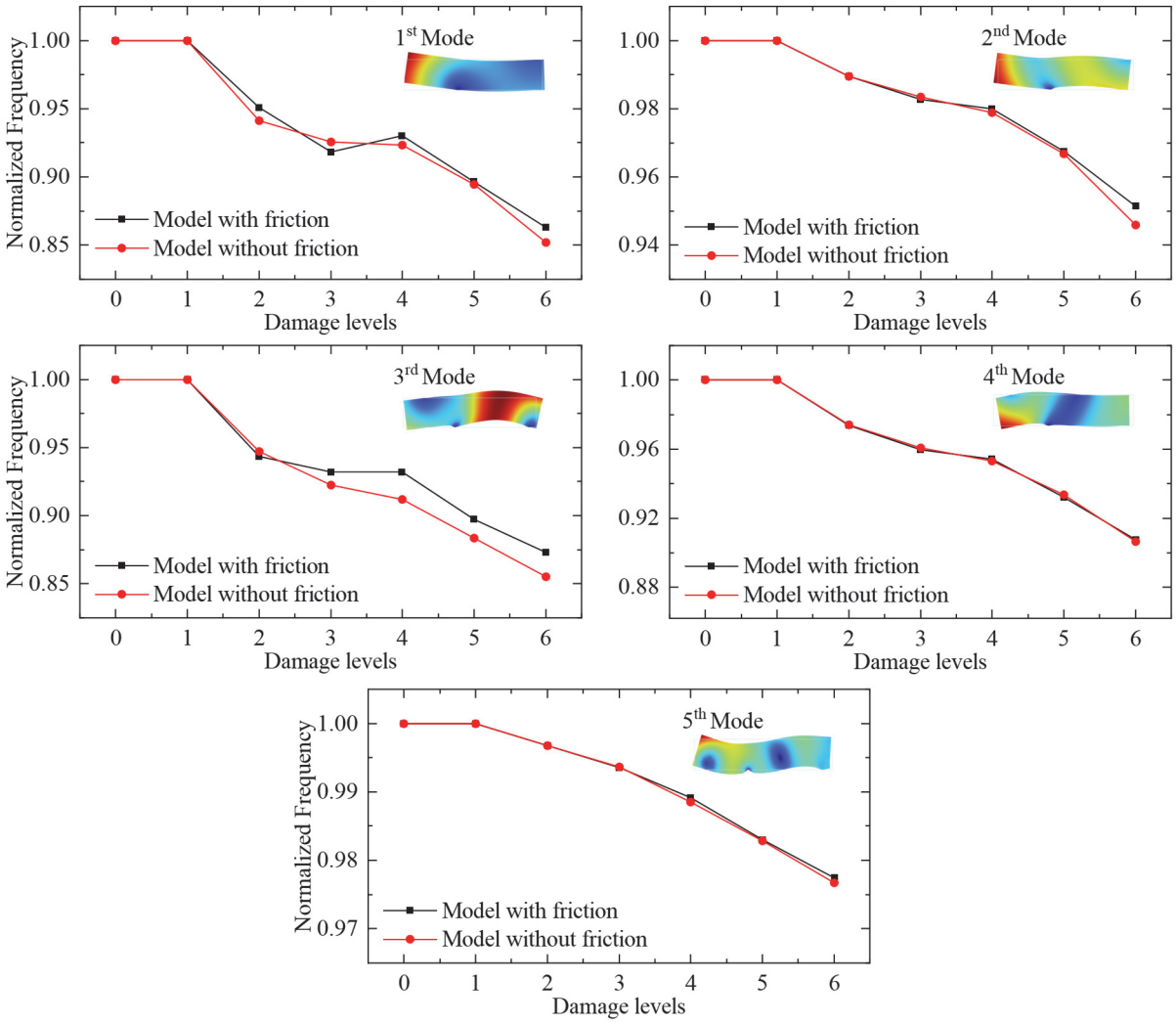

Figure 8: Normalized frequencies as the damage levels increase, of all investigated mode shapes: effects of the friction contribution on the cohesive mode II traction-separation law.

Afterwards, the MAC coefficients have been evaluated through Eqn. (9) and reported in Tab. 6. As can be seen, perfect correspondence occurs only for the first load level; in fact, in this case, all contributions along the diagonal are equal to 1. On the other hand, as the damage level increases, the values of the diagonal coefficients deviate more and more from the unit value. Furthermore, the same table highlights the growing inconsistency between some of the analyzed mode shapes; in particular, the off-diagonal coefficients indicating the correlation between modes 2 and 5 decrease as the damage level increases, settling at zero from level L4' onwards.

In addition, the Modal Curvature (MC) for each vibration mode has been evaluated by using the previously explained Eqn. (10). In particular, 31 reference points, 11.25 mm equally spaced, have been located along the upper edge of the specimen, as depicted in Fig. 6a. Fig. 9 shows the obtained modal curvatures for the first 5 modes as the damage level increases. We can note that the variations of curvature values are concentrated in the region where the damage phenomena occur. Furthermore, the loading conditions imposed on the specimen lead to frictional forces that contribute to the expansion of the damaged area beyond the immediate vicinity of the macro crack. This broader understanding underscores the complexity

of structural deterioration and highlights the importance of comprehensive assessment methods in ensuring the reliability and safety of the material under consideration.

Undamaged – L1’				
1.0000	0.3658	0.1074	0.0137	0.0026
0.3658	1.0000	0.2882	0.0014	0.0009
0.1074	0.2882	1.0000	0.0815	0.0003
0.0137	0.0014	0.0815	1.0000	0.8299
0.0026	0.0009	0.0003	0.8299	1.0000
Undamaged – L2’				
1.0000	0.3926	0.1089	0.0144	0.0024
0.3711	1.0000	0.2880	0.0020	0.0007
0.1040	0.2635	0.9997	0.0871	0.0001
0.0139	0.0012	0.0749	0.9998	0.8419
0.0023	0.0006	0.0007	0.8272	0.9997
Undamaged – L3’				
0.9997	0.3602	0.1177	0.0585	0.0019
0.3533	0.9994	0.2781	0.0004	0.0001
0.1145	0.2913	0.9962	0.1078	0.0004
0.0148	0.0015	0.0585	0.9583	0.8715
0.0021	0.0007	0.0031	0.8199	0.9958

Undamaged – L4’				
0.9997	0.2021	0.1538	0.1582	0.0016
0.3501	0.9645	0.2308	0.0234	0.0000
0.1172	0.4610	0.9895	0.1187	0.0013
0.0139	0.0036	0.0578	0.8214	0.8821
0.0028	0.0033	0.0036	0.6296	0.9929
Undamaged – L5’				
0.9998	0.2444	0.1303	0.2220	0.0015
0.3520	0.9811	0.2597	0.0112	0.0000
0.1159	0.4121	0.9952	0.2388	0.0010
0.0141	0.0027	0.0613	0.7332	0.8739
0.0026	0.0027	0.0028	0.4332	0.9949
Undamaged – L6’				
0.9997	0.2405	0.1307	0.4954	0.0012
0.3495	0.9792	0.2589	0.0506	0.0000
0.1174	0.4151	0.9944	0.3144	0.0018
0.0144	0.0022	0.0601	0.2252	0.8802
0.0025	0.0033	0.0030	0.0458	0.9933

Table 6: Modal Assurance Criterion (MAC) for the investigated damage levels with respect to the undamaged configurations for the non-symmetric three-point bending test.

Additionally, the curves associated with the higher vibration modes present increasingly complex oscillatory trends; such behavior is most emphasized for the fifth vibration mode shape (see Fig. 9). As a matter of fact, as the level of damage increases, beyond the peak point at which the coalescence of different micro-cracks into a single macro-crack occurs, the curves deviate more and more from that representing the undeformed condition. It is important to remind, however, that the undamaged condition and the condition associated with the L1’ level, represented by the orange and black lines in Fig. 9 respectively, are completely overlapping since, as can be seen from the displacement-load curve (Fig. 7), the first unloading path has been carried out for a displacement value that is still associated to a linear-elastic behavior.

Conclusions

In the present work, an improved numerical model to investigate the crack-induced degradation of the vibration characteristics in plain concrete structures has been presented. In particular, proper traction-separation laws adapted for cycling loading conditions including frictional effects, have been developed in order to capture the complex non-linear phenomena induced by the load application, such as such as concrete plasticity, partial closure of the cracks, and aggregate interlocking. The proposed numerical method has been employed for two different numerical applications, a symmetric and a non-symmetric three-point bending test in order to analyze the structural behavior under mode-I and mixed-mode fracture conditions, respectively.

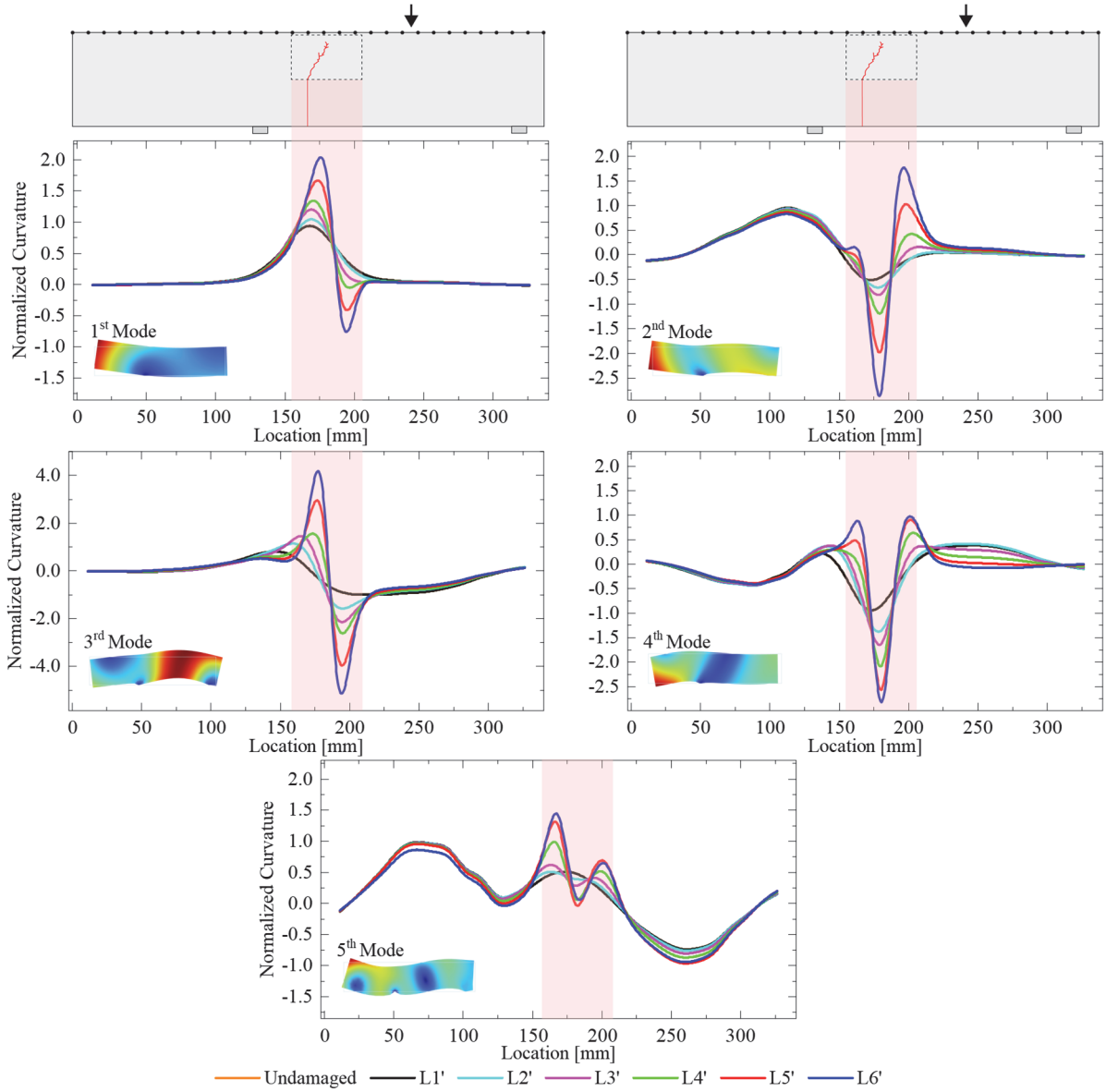

Figure 9: Modal Curvature (MC) damage factor of the first five mode shapes for all the investigated damage levels at the unloading phase (no-symmetric three-point bending test).

The load-carrying capacity is predicted by performing a quasi-static analysis until the complete failure of the considered specimen. 6 unloading paths, from L1' to L6' have been performed starting to different load levels taken as a percentage of the failure load. At the final point of such unloading paths, associated with a zero value of the applied load, the eigenvalue problem for free oscillations of small amplitude has been solved, thus assessing the natural vibration frequencies. In the mode-I fracture analysis, the results showed a maximum reduction of the natural frequencies of approximately 7.40% for the 5th vibration mode. Furthermore, the evolution of the damage is such that it produces a progressive monotonic degradation of the vibration frequencies only for the odd-numbered modes. Such behavior is related to the fact that these modes, as shown by the deformed modal shapes in Fig. 8, involve the area in which the damage can develop, thus generating a mode-I progressive fracture growth.

On the other hand, for the mixed mode fracture test, a different behavior has been found, such that the highest value of frequency reductions, around 13.69% and 12.70%, have been registered for mode 1 and mode 3 respectively, due to the non-symmetric boundary conditions imposed on the specimen. For this test, a comparison between the proposed model incorporating friction effects and the same model but without friction effects, was conducted. The results showed that, with the exception of some vibration modes that involve the free portion of the beam and do not affect the area within which the damage may grow, the natural vibration frequencies associated with the frictionless model are lower than those in which this effect has been taken into account; this results in less stiff elements that exhibit greater degradation of their own

vibration frequencies as the level of damage increases and for higher vibration mode shapes. Finally, the MAC- and MC-based damage detection methods are used in order to establish a correlation between the undamaged/damaged vibration modes and to define the magnitude and location of damage for the different mode shapes.
The obtained results have highlighted the computational capabilities of the proposed method to predict the static and dynamic structural behavior of plain concrete elements demonstrating its applicability in the framework of structural health monitoring. As a future perspective of this work, the proposed strategy could be inserted in a multiscale framework to capture the microscale effects induced by micro-crack evolutions and geometrical instabilities as rescontrated in composite materials [50,51]

ACKNOWLEDGEMENTS

Fabrizio Greco and Umberto De Maio gratefully acknowledge the financial support from the Next Generation EU-Italian NRRP, Mission 4, Component 2, Investment 1.5, call for the creation and strengthening of "Innovation Ecosystems", building "Territorial and R&D Leaders" (Directiorial Decree n. 2021/3277)-project Tech4You-Technologies for climate change and adaption and quality of life improvement, n. ECS0000009; Andrea Pranno gratefully acknowledges financial support from the POR Calabria FESR-FSE 2014-2020, Rep. N. 1006 of 30/30/2018, Line B, Action 10.5.12.

REFERENCES

[1] Karbhari, V.M., Lee, L.S.-W. (2009).Vibration-based damage detection techniques for structural health monitoring of civil infrastructure systems. Structural Health Monitoring of Civil Infrastructure Systems, Elsevier, pp. 177–212.
[2] Tatipala, S., Wall, J., Johansson, C., Larsson, T. (2020). A Hybrid Data-Based and Model-Based Approach to Process Monitoring and Control in Sheet Metal Forming, Processes, 8(1), pp. 89, DOI: 10.3390/pr8010089.
[3] Svendsen, B.T., Frøseth, G.T., Øiseth, O., Rønnquist, A. (2022). A data-based structural health monitoring approach for damage detection in steel bridges using experimental data, J. Civ. Struct. Heal. Monit., 12(1), pp. 101–115, DOI: 10.1007/s13349-021-00530-8.
[4] Fugate, M.L., Sohn, H., Farrar, C.R. (2001). Vibration-based damage detection using statistical process control, Mech. Syst. Signal Process., 15(4), pp. 707–721, DOI: 10.1006/mssp.2000.1323.
[5] Abdel Wahab, M.M., De Roeck, G. (1999). Damage detection in bridges using modal curvatures: application to a real damage scenario, J. Sound Vib., 226(2), pp. 217–235, DOI: 10.1006/jsvi.1999.2295.
[6] Entezami, A., Shariatmadar, H. (2018). An unsupervised learning approach by novel damage indices in structural health monitoring for damage localization and quantification, Struct. Heal. Monit., 17(2), pp. 325–345, DOI: 10.1177/1475921717693572.
[7] Catbas, F.N., Gokce, H.B., Gul, M. (2012). Nonparametric analysis of structural health monitoring data for identification and localization of changes: Concept, lab, and real-life studies, Struct. Heal. Monit., 11(5), pp. 613–626, DOI: 10.1177/1475921712451955.
[8] Zhang, C., Mousavi, A.A., Masri, S.F., Gholipour, G., Yan, K., Li, X. (2022). Vibration feature extraction using signal processing techniques for structural health monitoring: A review, Mech. Syst. Signal Process., 177, pp. 109175, DOI: 10.1016/j.ymssp.2022.109175.
[9] Goyal, D., Pabla, B.S. (2016). The Vibration Monitoring Methods and Signal Processing Techniques for Structural Health Monitoring: A Review, Arch. Comput. Methods Eng., 23(4), pp. 585–594, DOI: 10.1007/s11831-015-9145-0.
[10] El Mountassir, M., Yaacoubi, S., Mourot, G., Maquin, D. (2018). Sparse estimation based monitoring method for damage detection and localization: A case of study, Mech. Syst. Signal Process., 112, pp. 61–76, DOI: 10.1016/j.ymssp.2018.04.024.
[11] Finotti, R.P., Cury, A.A., Barbosa, F. de S. (2019). An SHM approach using machine learning and statistical indicators extracted from raw dynamic measurements, Lat. Am. J. Solids Struct., 16(2), DOI: 10.1590/1679-78254942.
[12] Worden, K., Manson, G. (2007). The application of machine learning to structural health monitoring, Philos. Trans. R. Soc. A Math. Phys. Eng. Sci., 365(1851), pp. 515–537, DOI: 10.1098/rsta.2006.1938.
[13] Sen, D., Nagarajaiah, S. (2018).Data-Driven Approach to Structural Health Monitoring Using Statistical Learning Algorithms., pp. 295–305.
[14] Gui, G., Pan, H., Lin, Z., Li, Y., Yuan, Z. (2017). Data-driven support vector machine with optimization techniques for structural health monitoring and damage detection, KSCE J. Civ. Eng., 21(2), pp. 523–534,

[15] DOI: 10.1007/s12205-017-1518-5.
[16] Rojo-Álvarez, J.L., Camps-Valls, G., Martínez-Ramón, M., Soria-Olivas, E., Navia-Vázquez, A., Figueiras-Vidal, A.R. (2005). Support vector machines framework for linear signal processing, Signal Processing, 85(12), pp. 2316–2326, DOI: 10.1016/j.sigpro.2004.12.015.
[17] Alves, V., Cury, A., Roitman, N., Magluta, C., Cremona, C. (2015). Novelty detection for SHM using raw acceleration measurements, Struct. Control Heal. Monit., 22(9), pp. 1193–1207, DOI: 10.1002/stc.1741.
[18] Ratton, L., Kunt, T., McAvoy, T., Fuja, T., Cavicchi, R., Semancik, S. (1997). A comparative study of signal processing techniques for clustering microsensor data (a first step towards an artificial nose), Sensors Actuators B Chem., 41(1–3), pp. 105–120, DOI: 10.1016/S0925-4005(97)80283-3.
[19] Doebling, S.W., Farrar, C.R., Prime, M.B. (1998). A Summary Review of Vibration-Based Damage Identification Methods, Shock Vib. Dig., 30(2), pp. 91–105, DOI: 10.1177/058310249803000201.
[20] Chaupal, P., Rajendran, P. (2023). A review on recent developments in vibration-based damage identification methods for laminated composite structures: 2010–2022, Compos. Struct., 311, pp. 116809, DOI: 10.1016/j.compstruct.2023.116809.
[21] Magalhães, F., Cunha, A., Caetano, E. (2012). Vibration based structural health monitoring of an arch bridge: From automated OMA to damage detection, Mech. Syst. Signal Process., 28, pp. 212–228, DOI: 10.1016/j.ymssp.2011.06.011.
[22] Yuen, M.M.F. (1985). A numerical study of the eigenparameters of a damaged cantilever, J. Sound Vib., 103(3), pp. 301–310, DOI: 10.1016/0022-460X(85)90423-7.
[23] Ostachowicz, W.M., Krawczuk, M. (1991). Analysis of the effect of cracks on the natural frequencies of a cantilever beam, J. Sound Vib., 150(2), pp. 191–201, DOI: 10.1016/0022-460X(91)90615-Q.
[24] Marfia, S., Monaldo, E., Sacco, E. (2022). Cohesive fracture evolution within virtual element method, Eng. Fract. Mech., 269, pp. 108464, DOI: 10.1016/j.engfracmech.2022.108464.
[25] De Maio, U., Greco, F., Lonetti, P., Pranno, A. (2024). A combined ALE-cohesive fracture approach for the arbitrary crack growth analysis, Eng. Fract. Mech., 301, pp. 109996, DOI: 10.1016/j.engfracmech.2024.109996.
[26] Pranno, A., Greco, F., Lonetti, P., Luciano, R., De Maio, U. (2022). An improved fracture approach to investigate the degradation of vibration characteristics for reinforced concrete beams under progressive damage, Int. J. Fatigue, 163, pp. 107032, DOI: 10.1016/j.ijfatigue.2022.107032.
[27] Bruno, D., Greco, F., Lonetti, P. (2009). Dynamic Mode I and Mode II Crack Propagation in Fiber Reinforced Composites, Mech. Adv. Mater. Struct., 16(6), pp. 442–455, DOI: 10.1080/15376490902781183.
[28] Greco, F. (2009). Homogenized mechanical behavior of composite micro-structures including micro-cracking and contact evolution, Eng. Fract. Mech., 76(2), pp. 182–208, DOI: 10.1016/j.engfracmech.2008.09.006.
[29] Greco, F., Leonetti, L., Nevone Blasi, P. (2012). Non-linear macroscopic response of fiber-reinforced composite materials due to initiation and propagation of interface cracks, Eng. Fract. Mech., 80, pp. 92–113, DOI: 10.1016/j.engfracmech.2011.10.003.
[30] Pham, T.M., Hao, H. (2016). Review of Concrete Structures Strengthened with FRP Against Impact Loading, Structures, 7, pp. 59–70, DOI: 10.1016/j.istruc.2016.05.003.
[31] Greco, F., Lonetti, P., Blasi, P.N. (2007). An analytical investigation of debonding problems in beams strengthened using composite plates, Eng. Fract. Mech., 74(3), pp. 346–372, DOI: 10.1016/j.engfracmech.2006.05.023.
[32] De Maio, U., Gaetano, D., Greco, F., Lonetti, P., Nevone Blasi, P., Pranno, A. (2023). The Reinforcing Effect of Nano-Modified Epoxy Resin on the Failure Behavior of FRP-Plated RC Structures, Buildings, 13(5), pp. 1139, DOI: 10.3390/buildings13051139.
[33] Bastos, G., Patiño-Barbeito, F., Patiño-Cambeiro, F., Armesto, J. (2016). Nano-Inclusions Applied in Cement-Matrix Composites: A Review, Materials (Basel)., 9(12), pp. 1015, DOI: 10.3390/ma9121015.
[34] Onaizi, A.M., Huseien, G.F., Lim, N.H.A.S., Amran, M., Samadi, M. (2021). Effect of nanomaterials inclusion on sustainability of cement-based concretes: A comprehensive review, Constr. Build. Mater., 306, pp. 124850, DOI: 10.1016/j.conbuildmat.2021.124850.
[35] Chen, G.M., Teng, J.G., Chen, J.F. (2011). Finite-Element Modeling of Intermediate Crack Debonding in FRP-Plated RC Beams, J. Compos. Constr., 15(3), pp. 339–353, DOI: 10.1061/(ASCE)CC.1943-5614.0000157.
[36] Mohamed Ali, M.S., Oehlers, D.J., Griffith, M.C. (2008). Simulation of Plastic Hinges in FRP-Plated RC Beams, J. Compos. Constr., 12(6), pp. 617–625, DOI: 10.1061/(ASCE)1090-0268(2008)12:6(617).
[37] Scorza, D., Luciano, R., Vantadori, S. (2022). Fracture behaviour of nanobeams through Two-Phase Local/Nonlocal Stress-Driven model, Compos. Struct., 280, pp. 114957, DOI: 10.1016/j.compstruct.2021.114957.
[38] Ammendolea, D., Greco, F., Lonetti, P., Luciano, R., Pascuzzo, A. (2021). Crack propagation modeling in functionally graded materials using Moving Mesh technique and interaction integral approach, Compos. Struct., 269, pp. 114005, DOI: 10.1016/j.compstruct.2021.114005.

[39] Neild, S.A., Williams, M.S., McFadden, P.D. (2002). Non-linear behaviour of reinforced concrete beams under low-amplitude cyclic and vibration loads, Eng. Struct., 24(6), pp. 707–18, DOI: 10.1016/S0141-0296(01)00134-1.
[40] Isaković, T., Fischinger, M. (2019). Assessment of a force–displacement based multiple-vertical-line element to simulate the non-linear axial–shear–flexure interaction behaviour of reinforced concrete walls, Bull. Earthq. Eng., 17(12), pp. 6369–6389, DOI: 10.1007/s10518-019-00680-7.
[41] Koh, S.J.A., Maalej, M., Quek, S.T. (2004). Damage Quantification of Flexurally Loaded RC Slab Using Frequency Response Data, Struct. Heal. Monit., 3(4), pp. 293–311, DOI: 10.1177/1475921704003004O1.
[42] Hanif, M.U., Ibrahim, Z., Jameel, M., Ghaedi, K., Hashim, H. (2021). Simulation-based non-linear vibration model for damage detection in RC beams, Eur. J. Environ. Civ. Eng., 25(8), pp. 1379–1404, DOI: 10.1080/19648189.2019.1578270.
[43] Van Den Abeele, K., De Visscher, J. (2000). Damage assessment in reinforced concrete using spectral and temporal nonlinear vibration techniques, Cem. Concr. Res., 30(9), pp. 1453–1464, DOI: 10.1016/S0008-8846(00)00329-X.
[44] Reinhardt, H.W. (1984). Fracture Mechanics of an Elastic Softening Material like Concrete, HERON, 29(2), DOI: http://resolver.tudelft.nl/uuid:7e908683-e816-4c4f-928f-03103ed2780e.
[45] Hamad, W.I., Owen, J.S., Hussein, M.F.M. (2015). Modelling the degradation of vibration characteristics of reinforced concrete beams due to flexural damage, Struct. Control Heal. Monit., 22(6), pp. 939–967, DOI: 10.1002/stc.1726.
[46] Bilbie, G., Dascalu, C., Chambon, R., Caillerie, D. (2008). Micro-fracture instabilities in granular solids, Acta Geotech., 3(1), pp. 25–35, DOI: 10.1007/s11440-007-0046-8.
[47] Petersson, P. (1981). Crack growth and development of fracture zones in plain concrete and similar materials, Eng. Mater. Sci. Rep. TVBM.
[48] Allemang, R. j., Brown, D.L. (1982).A Correlation Coefficient for Modal Vector Analysis. Proceedings of the 1st International Modal Analysis Conference, pp. 110–116.
[49] Pandey, A.K., Biswas, M., Samman, M.M. (1991). Damage detection from changes in curvature mode shapes, J. Sound Vib., 145(2), pp. 321–332.
[50] Gálvez, J., Elices, M., Guinea, G., Planas, J. (1998). Mixed Mode Fracture of Concrete under Proportional and Nonproportional Loading, Int. J. Fract., 94, pp. 267–284, DOI: 10.1023/A:1007578814070.
[51] Greco, F., Leonetti, L., Nevone Blasi, P. (2014). Adaptive multiscale modeling of fiber-reinforced composite materials subjected to transverse microcracking, Compos. Struct., 113, pp. 249–263, DOI: 10.1016/j.compstruct.2014.03.025.
[52] Greco, F. (2013). A study of stability and bifurcation in micro-cracked periodic elastic composites including self-contact, Int. J. Solids Struct., 50(10), pp. 1646–1663, DOI: 10.1016/j.ijsolstr.2013.01.036.